optica

Low-threshold polariton lasing in a highly disordered conjugated polymer: supplementary material

MENGJIE WEI, SAI KIRAN RAJENDRAN, HAMID OHADI, LAURA TROPF, MALTE C. GATHER, GRAHAM A. TURNBULL*, AND IFOR D. W. SAMUEL*

Organic Semiconductor Centre, SUPA, School of Physics and Astronomy, University of St Andrews, St Andrews, KY16 9SS, UK
**Corresponding author: gat@st-andrews.ac.uk; idws@st-andrews.ac.uk*

Published 27 August 2019

This document provides supplementary information to "Low-threshold polariton lasing in a highly disordered conjugated polymer," https://doi.org/10.1364/OPTICA.6.001124. It includes the calculation of the cavity finesse, quality factor and photon lifetime, angle-resolved reflectivity spectra from 40° to 74°, coupled oscillator model description of strong exciton-photon coupling in poly(9,9-dioctylfluorene) microcavity, transfer matrix simulation of reflectivity dispersion, angle-resolved photoluminescence in logarithmic scale, thermalization of lower polaritons, real-space images from single arm and two arms of Michelson interferometer at three different excitation densities, and the interference pattern with enlarged pump laser beam.

1. CALCULATION OF CAVITY FINESSE, QUALITY FACTOR AND PHOTON LIFETIME

The finesse of microcavities is calculated based on the following equation

$$F = \frac{\pi(R_1R_2)^{1/4}}{1-(R_1R_2)^{1/2}}, \quad \text{(S1)}$$

where R_1 and R_2 are the estimated reflectivity of the bottom and top distributed Bragg reflectors (DBRs). The minimum transmission of the bottom and top DBRs was measured to be 0.7% and 1.8%, respectively. The cavity finesse is calculated to be 244 using the values of 99.3% and 98.2% as the maximum reflectivity of the bottom and top DBRs.

The cavity quality factor Q is given by

$$Q = \frac{2\pi d}{\lambda_0}\frac{(R_1R_2)^{1/4}}{1-(R_1R_2)^{1/2}} \quad \text{(S2)}$$

where d is the optical distance between the two mirrors and λ_0 is the resonant wavelength of the cavity. Since a $\lambda_0/2$ cavity was studied in this work, the Q is equal to the cavity finesse F (= 244).

The photon lifetime inside the cavity is given by

$$\tau_p = \frac{2d/c}{1-R_1R_2} \quad \text{(S3)}$$

For the reflectivity of the DBRs mentioned above, the intra-cavity photon lifetime is ~ 69 fs.

2. ANGLE-RESOLVED REFLECTIVITY SPECTRA

To clearly show the strong coupling evidence, we plot out angle-resolved reflectivity spectra from 40° to 74° measured by ellipsometer in Fig. S1. The two sets of drifting dips around 2.9 eV and 3.6 eV are identified as the lower and upper polariton branches, respectively. The anti-crossing dispersion reflects the emergence of strong coupling between excitons and cavity photons.

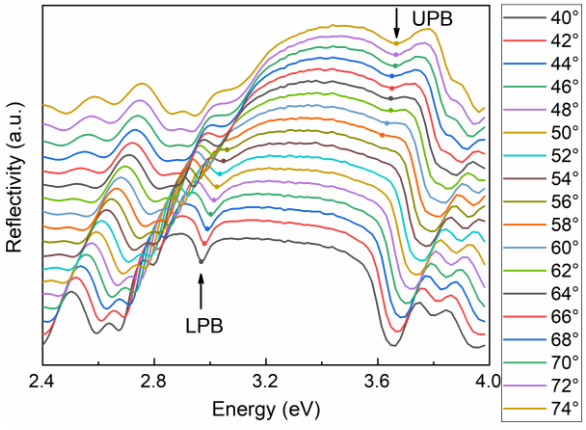

Fig. S1. Angle-resolved reflectivity spectra from 40° and 74° of the microcavity measured by ellipsometer. The spectra are vertically translated to enhance visibility of features. The positions of reflectivity dips are marked by scatters.

3. COUPLED OSCILLATOR MODEL

The strong exciton-photon coupling in the microcavity can be described by a standard coupled oscillator model

$$\begin{pmatrix} E_{ph}(0)\left(1-\frac{sin^2\theta}{n_{eff}^2}\right)^{-1/2} & V \\ V & E_{exc} \end{pmatrix}\begin{pmatrix}\alpha\\ \beta\end{pmatrix} = E\begin{pmatrix}\alpha\\ \beta\end{pmatrix}. \quad \textbf{(S4)}$$

where $E_{ph}(0)$ is the cutoff energy of uncoupled photon at $k_{//} = 0$, θ is the incident angle, n_{eff} is the effective refractive index in the cavity, V is the interaction strength between exciton and cavity photon and E_{exc} is the uncoupled exciton energy. The eigenvalues E of this matrix are used to fit the measured dispersion of the lower and upper polariton branches (LPB and UPB). The best fitting parameters are listed in Fig. 2. The calculated dispersion relation shows good agreement with both the reflectivity and photoluminescence (PL) dispersions in Fig. 2 and Fig. 3. From the coupled oscillator model, the Hopfield coefficients indicate the excitonic and photonic fractions of the LPB and UPB are also determined as shown in Fig. S2. The magnitudes α^2 and β^2 correspond to the photonic fraction and excitonic fraction of polariton wavefunctions. At $k_{//} = 0$, the LPB consists of 72% photonic and 28% excitonic contributions.

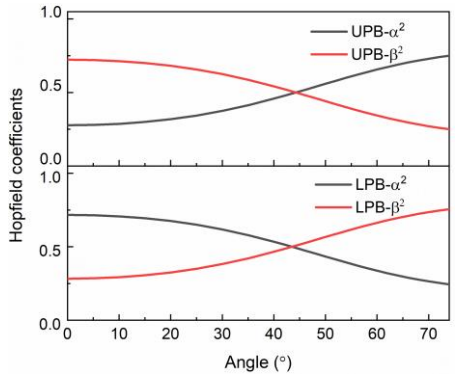

Fig. S2. The Hopfield coefficients extracted from the coupled oscillator model. The bottom and top parts correspond to calculations for the LPB and UPB, respectively.

4. TRANSFER MATRIX CALCULATION

The experimentally observed angular reflectivity was further compared with simulation data obtained from transfer matrix calculations. The complex refractive index of poly(9,9-dioctylfluorene), as shown in Fig. S3, and film thickness used in the calculation were measured by spectroscopic ellipsometry. Figure S4(a) shows the contour map and symbols indicative of the calculated and measured angle-resolved reflectivity, respectively. To see details, especially for the UPB, we also plot out reflectivity minima of calculated and measured dispersions at each angle as shown in Fig. S4(b). The calculated dispersions agree well with the experimental data.

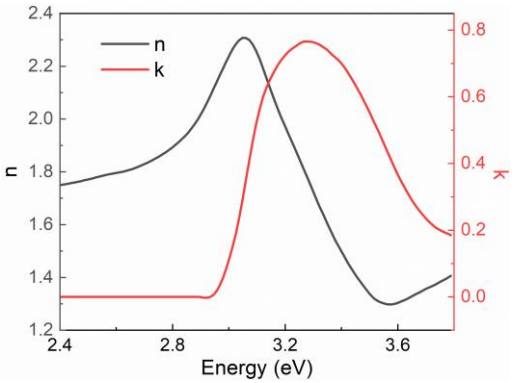

Fig. S3. The refractive index and extinction coefficient of poly(9,9-dioctylfluorene) film.

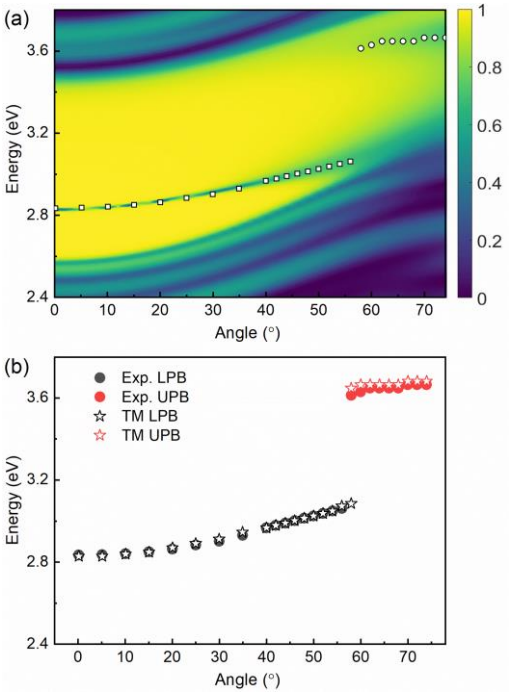

Fig. S4. (a) Transfer matrix calculation of polariton dispersion relations. The open squares and circles indicate the measured dispersion of the LPB and UPB, respectively. (b) Black and red circles correspond to measured reflectivity minima at each angle, while black and red stars are reflectivity minima taken from transfer matrix calculations at corresponding angles.

5. ANGLE-RESOLVED PHOTOLUMINESCENCE AND REAL-SPACE IMAGE IN LOGARITHMIC SCALES

Figure S5 shows the same power-dependent angle-resolved PL and real-space images as in Fig. 3 but in false color logarithmic scale. It shows the same trend as in Fig. 3. Below threshold (Fig. S5(a)), the lower polariton population spread along the branch and the emission is most intense at $k_{//}=0$. On increasing pump fluence (Fig. S5(b)), the angle range with intense emission slightly narrows. Once above threshold (Fig. S5(c)), most of lower polaritons occupy the bottom of the branch with emission intensity 2 to 3 magnitudes higher than that of emission at large angles. Figures (d)-(f) are real-space images. Apparently, the core of emission spot shrinks to a smaller one when above threshold as explained in main text.

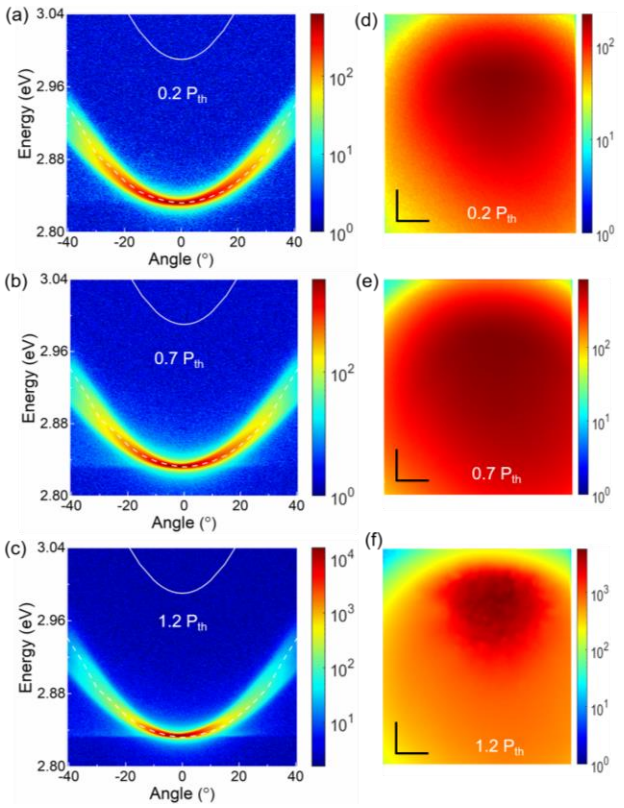

Fig. S5. Power-dependent angle-resolved PL spectra in Fourier-space and real-space images in logarithmic scales. Each of panels corresponds to panels in Fig. 3 in the same order. The left panel (a)-(c) are lower polariton emission as a function of angle at incident pump fluence of 4.3 μJ/cm² (0.2 P_{th}), 19.7 μJ/cm² (0.7 P_{th}) and 33.8 μJ/cm² (1.2 P_{th}). The dashed white lines indicate the measured lower polariton dispersion and the solid white lines refer to the uncoupled cavity mode. The right panel (d)-(f) are real-space images with corresponding excitation densities. The scale bars are 20 μm.

6. THERMALIZATION OF LOWER POLARITONS

Figure S6 shows the lower polariton occupation as a function of energy at different pump fluences. The polariton occupancy $n(E_k)$ is fitted to classic Maxwell-Boltzmann (MB) distribution

$$n(E_k) \propto e^{\frac{-(E_k - E_{k//=0})}{k_b T}} \quad \text{(S5)}$$

At 0.2 P_{th}, the occupancy follows a MB distribution reasonably well. On increasing excitation density to 0.7 P_{th}, the occupancy at low energy states cannot be simply fitted by MB distribution, which may be caused by the onset of massive occupation at the bottom of the branch when close to polariton lasing threshold. This behavior becomes more apparent at threshold. We note that the occupancy is not fully thermalized because the system is not at equilibrium as discussed in a former work on polymer polariton lasing [1]. Above threshold, we see the massive occupation at the bottom of the lower polariton branch which is consistent with polariton lasing. Effective temperatures of between 310 K and 240 K were obtained for polariton occupancies at the range of excitation densities shown in Fig. S6.

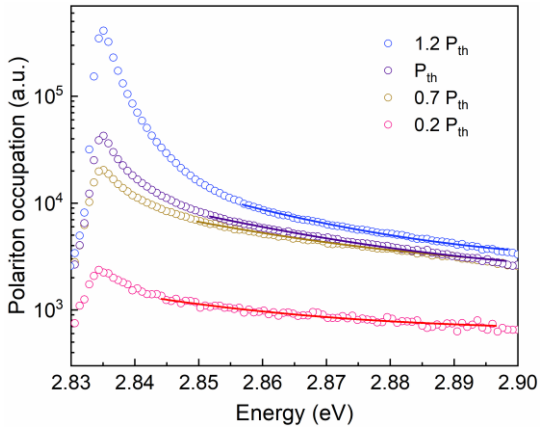

Fig. S6. Lower polariton occupations as a function of energy at different excitation densities. All occupation curves are fitted to Maxwell-Boltzmann distribution.

7. SPATIAL COHERENCE MEASUREMENT

To have a clear picture about the real-space emission from each arm with increasing excitation power, the images recorded for a range of pump fluences are plotted in Fig. S7. Below threshold (9.9 μJ/cm²), the entire pump region shows emission with low intensity in Fig. S7(a) and (b). When increasing the pump fluence (18.3 μJ/cm²) near to its threshold value, the polariton emission starts to lase at the center of the excitation spot because of the Gaussian pump beam profile, leading to interference patterns most visible in the center of Fig. S7(f). When the pump fluence is above threshold at 27.5 μJ/cm², the entire pump region exhibits polariton lasing properties. Comparing Fig. S7(g) and (h), two emission spots from the two arms of interferometer are evident, spatially separated by ~ 10 μm. An interference pattern is observed across the entire emission region in Fig. S7(i), indicating the build-up of long-range spatial coherence across a distance of 10 μm.

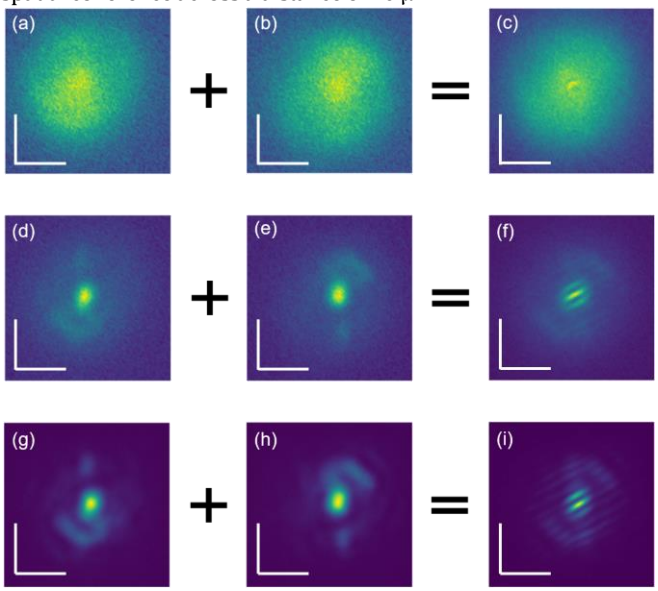

Fig. S7. (a), (d) and (g) show real space photoluminescence images from one arm of Michelson interferometer measured below, at and above threshold, respectively. (b), (e) and (h) are corresponding inverted images from the other arm of interferometer. (c), (f) and (i) are interferograms, the same as those shown in Fig. (5). All scale bars, 5 μm.

For the small pump spot used in the coherence measurement as shown in Fig. S7, the coherence length is limited by the pump size. This is supported by measurement of the spatial coherence with a

larger pump beam with a diameter of 41 μm. As shown in Fig. S8, although the intensity of emission from each arm is not uniform, the interference patterns show high visibility over a distance of 18 μm. The observed results also agree well with the reports of Daskalakis et al. in 2015 [2].

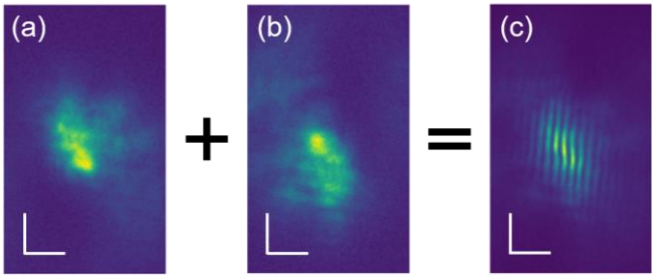

Fig. S8. (a) Above threshold real-space photoluminescence image from one arm of a Michelson interferometer using a Gaussian pump with a diameter of 41 μm. (b) Inverted image of (a) from the other arm. (c) Interferogram from the two arms of the interferometer. All scale bars are 5 μm.

References

1. J. D. Plumhof, T. Stoeferle, L. Mai, U. Scherf, and R. Mahrt, "Room-temperature Bose–Einstein condensation of cavity exciton–polaritons in a polymer," Nat. Mater. **13**, 328–9 (2014).
2. K. S. Daskalakis, S. A. Maier, and S. Kénna-Cohen, "Spatial Coherence and Stability in a Disordered Organic Polariton Condensate," Phys. Rev. Lett. **115**, 1–5 (2015).